



**INSTITUTE OF ORGANIC  
CHEMISTRY WITH CENTRE  
OF PHYTOCHEMISTRY**  
BULGARIAN ACADEMY OF SCIENCES



PhD candidate: **Consolato Rosmini**

**Advanced iron and nickel based materials for the safe  
production and storage of hydrogen**

**<<< AUTOR'S THESIS ABSTRACT >>>**

for awarding the educational and scientific degree "**doctor**"

**Supervisor:**

Prof. DSc Tanya Tsoncheva

**Co-supervisor:**

Prof. Dr. Nartzislav Petrov

Sofia, 2022

The PhD Thesis contains 177 pages. It includes 84 Figures, 4 Schemes, and 19 Tables. The results are published in 3 scientific publications.

The PhD Thesis will be discussed at the session of the "Functional Materials, Computer Modeling and Technologies" that will be held on 11.10.2022. The PhD student was enrolled in a form of self-education at the Institute of Organic Chemistry with Centre of Phytochemistry, Bulgarian Academy of Sciences in July 2021.

The experiments on the thesis are done at IOCCP-BAS, lab. "Organic Reaction on Microporous Materials", the Norwegian Institute of Technology, Norway, and the Institute of Carbochemistry in Zaragoza, Spain.

The defense of the thesis will be held on the 17<sup>th</sup> January 2023 at 10:00 o'clock at the IOCCP-BAS at a meeting of the scientific jury.

Jury members/reviewers:

- 1.
- 2.
- 3.
- 4.
- 5.

Reserve members:

- 1.
- 2.

All the documents on the thesis defense are available at the office of IOCCP-BAS and online on the webpage of the IOCCP-BAS.

## **INTRODUCTION:**

In recent years the need to convert our energy production currently focused on fossil fuels, into other sustainable and ecological production systems, has opened the way to a multitude of techniques and solutions based on the production of hydrogen as an energy carrier and possible clean solution to current energy problems. Hydrogen has several attractive features, beyond the obvious of being perfectly clean-burning and a very common element (though often tied up inconveniently with other elements such as oxygen or carbon). Of particular importance are its useful features of relative transportability (e.g. compared to heat) and long-term storability. Despite being a naturally occurring gas, currently the production of hydrogen presents numerous problems and limitations both from an ecological and economical point of view. In fact, the bulk of the hydrogen produced in the world is made from fossil fuels. Oil, naphtha, and natural gas are still the main materials used. Owing to their growing scarcity, some effort is being made to use the more abundant coal, although the high sulfur content of many coals leads to serious ecological concerns. Only 4% of hydrogen is produced by electrolysis of water, the remaining 96% is produced by hydrocarbon reforming processes.

In the last decades, research in the sector has concentrated with great effort on the development of new techniques for the production of hydrogen completely disconnected from the use of fossil fuels. Alternative production methods can be divided into two large macro-categories, biomass-based ones (e.g. gasification, pyrolysis, and aqueous phase reforming) and those operating by direct water splitting (e.g. electrolysis, photoelectrolysis, and thermochemical water splitting) however, specifying that the constant development of research on the subject annually leads to different production approaches and increasingly niche reactions.

Of the vastness of arguments arising from the treatment of these topics, this thesis takes on the task of exploring in greater detail two biomass-based techniques such as the Vapor Phase Reforming of methanol (Methanol Decomposition, MD) and the Aqueous Phase Reforming of ethylene glycol (APR-EG). Moreover, it will present a rational procedure in the production of catalysts useful for hydrogen production mechanisms through electrolysis, and specifically in the Oxygen Evolution Reaction (OER), notably the "bottleneck" half reaction of the "water splitting" reaction.

## **AIMS AND OBJECTIVES OF THE RESEARCH:**

This thesis aims to the synthesis of advanced mesoporous composites with tunable texture, surface and redox properties, based on abundance and low-cost metal/ metal oxides (Ni, Fe, Sn, Ce, Zr). The study is extended to the testing of these materials as catalysts for the production of hydrogen by different methods, such as decomposition of methanol, aqueous phase reforming (APR) of ethylene glycol and the reuse of waste catalysts from the methanol decomposition (MD) process, in the electro catalytic semi-reaction of Oxygen Evolution Reaction (OER) in an alkaline environment, in order to evaluate their possible use in the electrolysis of water in an alkaline environment.

In order to achieve the set goal, the following specific tasks are performed:

1. Template assisted hydrothermal synthesis and physicochemical characterization of mesoporous cerium-iron mixed oxides. Clarification of the effect of the preparation procedure by using different precipitating agents (ammonia or urea), variations in the solvent and the conditions for the template release.
2. Investigation of the influence of the Fe/Ce molar ratio on the phase composition and the related physicochemical and catalytic properties of cerium-iron mixed oxide nanocomposites.
3. Synthesis and physicochemical characterization of nickel modified iron-cerium mixed oxides nanocomposites. Investigation of the possible control of the state of the nickel phase by variation of the Fe-Ce support composition.
4. Elucidation of the influence of the porous structure of the ceria supports on the formation of the active centers in iron-cerium oxide catalyst and elucidations regarding the active centers in the tri-metallic catalysts in Fe-Ce-Ni.
5. Synthesis and physicochemical characterization of mesoporous Ce-Fe-Ni nanocomposites encapsulated in carbon-nanofibers. Investigation concerning the catalytic behavior in the Oxygen Evolution Reaction in an alkaline environment.
6. Synthesis and physicochemical characterization of Sn-Ni alloys supported on mesoporous cerium-zirconium mixed oxide. Clarification of the phase composition on the textural and structural properties.
7. Investigation of the influence of the variation in the metal content of Ni/Sn, for the formation of different Sn-Ni alloys supported on cerium-zirconium mixed oxide and the related physicochemical and catalytic properties in the Aqueous Phase Reforming reaction of ethylene glycol in batch reactor in standard and alkaline medium.

## <<< **RESULTS AND DISCUSSION** >>>

### **1. Influence of the Fe / Ce molar ration and synthetic procedures on the chemical-physical and catalytic properties for the methanol decomposition reaction.**

#### *1.1. Methods of preparation and physicochemical characterization of Fe-Ce binary oxides.*

A series of cerium–iron oxides with an Fe/Ce molar ratio between 1:9 and 9:1 were prepared using a template-assisted hydrothermal technique. The obtained product was filtered, washed with distilled water, and dried under ambient temperature. The template was released by calcination of the solid in air at 773 K for 10 h. The selected sample with an Fe/Ce ratio of 3:7 was calcined at 573 K. All these materials were denoted as xFeyCe\_HT(T), where x/y is the Fe/Ce mol ratio and T is the temperature of calcination in Kelvin. The procedure described above was modified using a mixture of 50 mL of distilled H<sub>2</sub>O and 10 mL of 95% ethanol for the solubilization of the metal precursors. Then, the template was released by calcination at 773 K and the sample was denoted as 3Fe7Ce\_Et(773). Alternatively, before the calcination at 773 K, the CTAB template was extracted by treatment with 95% ethanol solution (sample 3Fe7Ce\_Extr(773)). For the selected sample (3Fe7Ce\_U(773)), during the precipitation procedure at 323K, ammonia was replaced by urea followed by hydrothermal treatment and calcination at 773K, as described above.

In Figure 2-A and B are presented XRD patterns of Fe-Ce oxides with different composition, which were prepared by template-assisted hydrothermal technique using ammonia as a precipitator and calcination temperature of 773 K and using the other synthetic procedures. The reflections at 28.5°, 33.1°, 47.8°, 56.3°, 59.0°, 69.7°, 76.6° and 79.1° 2 $\theta$  in the pattern of CeO<sub>2</sub> were assigned to (111), (200), (220), (311), (222), (400), (331) and (420) lattice planes, respectively, of well-crystallized ceria (JCPDS 65-5923). These features appeared in the XRD patterns of all Fe-Ce binary oxides indicating preservation of the cubic fluorite structure. In case of the binary materials, the reflections became broader and less intensive. This indicated improvement in the ceria dispersion, which was more pronounced with the increase of iron content in the samples.

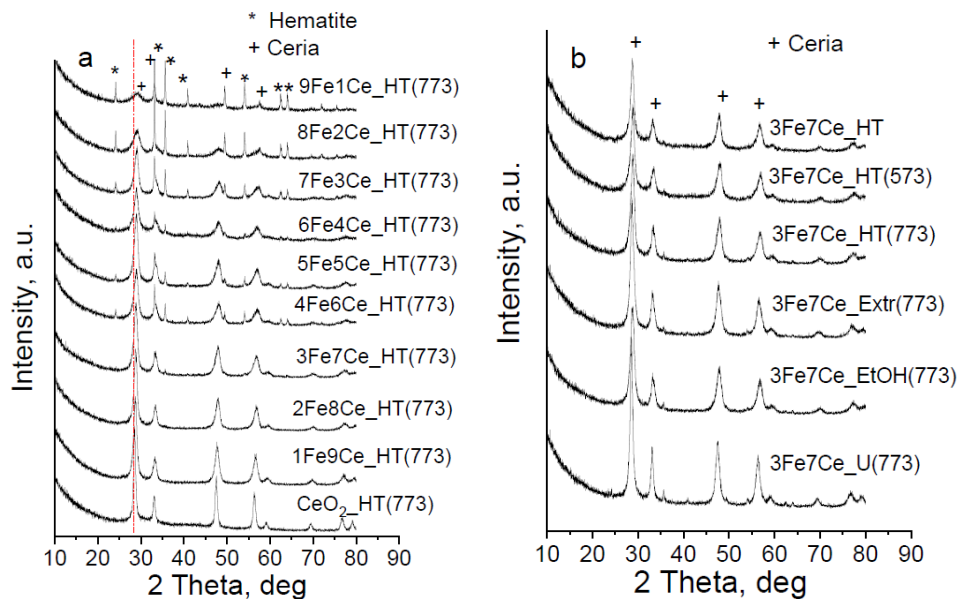


**Figure 2.** XRD patterns of ceria iron oxide materials with (a) different composition and (b) 3Fe7Ce\_HT prepared by variation in the preparation conditions.

The addition of high molar iron concentrations inside the ceria leads to the lowering of the surface area and the segregation of hematite particles interconnected to the ceria through Fe-O-Ce bridging bonds.

The High Resolution TEM (HRTEM) images (Figure 3-A) confirmed the predominant presence of nanoparticles of about 5 nm and small number of larger (10-15 nm) crystallites. Particles of different sizes and morphology can be distinguished. The larger particles with interplanar spacing of 0.365 and 0.247 nm were assigned to (012) and (110) planes of Fe<sub>2</sub>O<sub>3</sub> and the small crystallites with interplanar spacing of about 0.31 nm were typical of CeO<sub>2</sub> (111) plane. The samples microstructure at atomic scale was better visualized by Scanning Transmission Electron Microscopy with High Angle Annular Dark Field Detection (STEM-HAADF) (Figure 3-B). Here, the predominantly homogeneously distributed Fe in ceria matrix co-existed with few distinct pure iron crystallites and iron-rich structures in close contact with ceria entities.

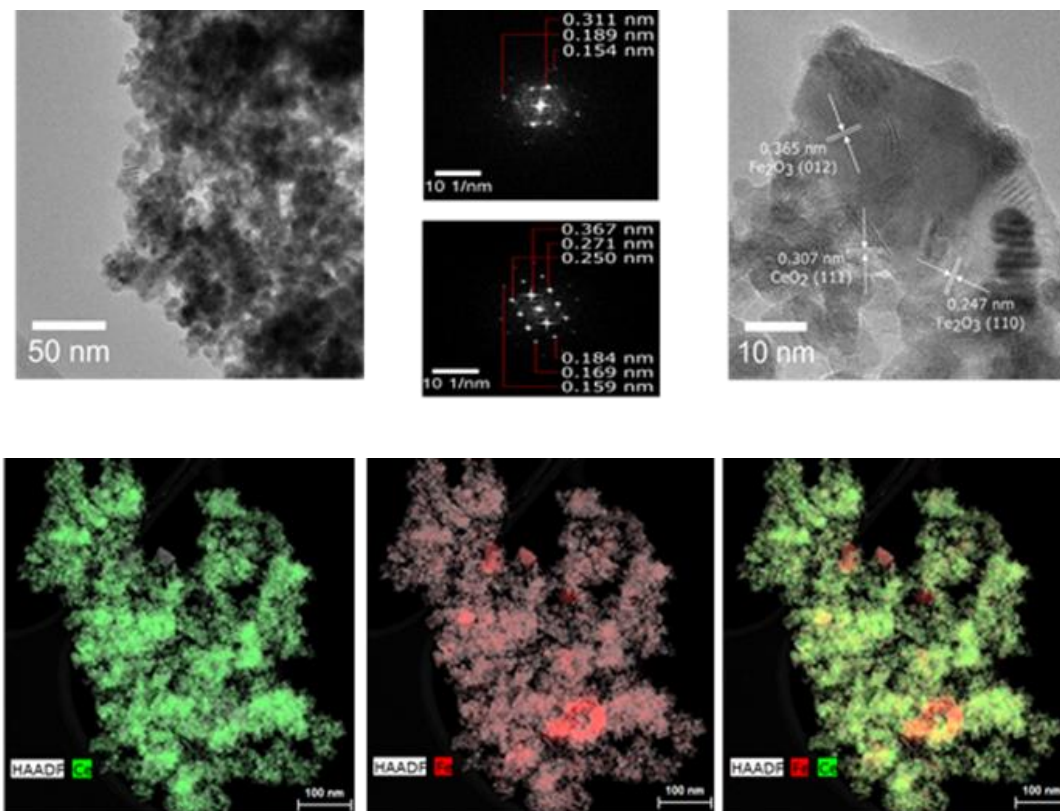


**Figure 3.** HRTEM (a) and HAADF-STEM (b) images for 5Fe5Ce\_HT(773).

The texture characteristics of the samples were investigated by low-temperature  $N_2$  physisorption (Figure 4). The adsorption-desorption isotherms were of type IV with well-defined hysteresis loop above 0.7-0.8 $P/P_0$  (Figure 4-A and B), typical of mesoporous materials.

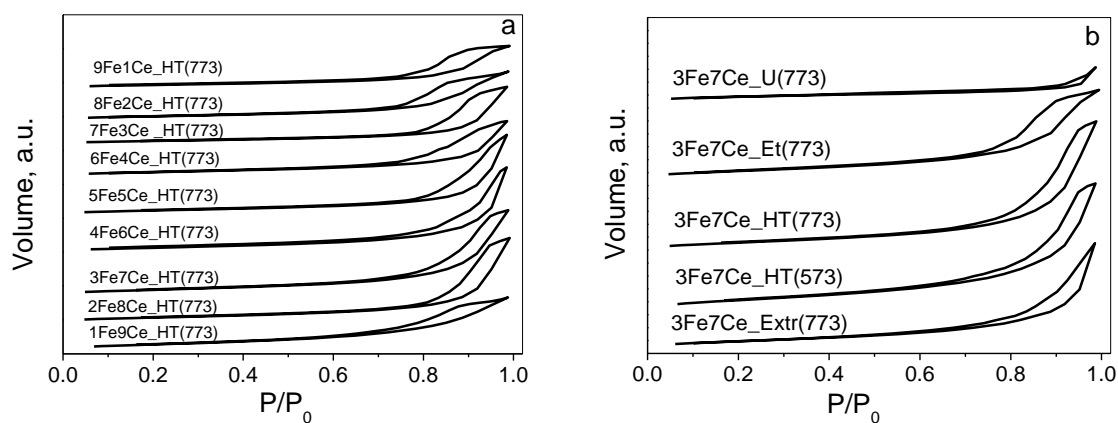


**Figure 4.** Nitrogen physisorption isotherms for selected ceria-iron oxides with different composition and calcined at 773K.

Moessbauer spectroscopy was used to obtain more information for the state of iron species in the composites (Figure 5). All room temperature Moessbauer spectra represented a superposition of sextets and doublets. The sextet component with isomer shift, quadrupole

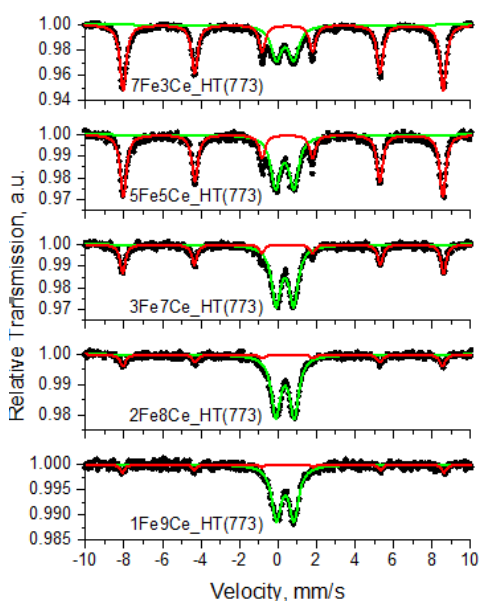


**Figure 5:** Moessbauer spectra of ceria iron oxide materials with different composition at RT.

shift, and hyperfine field of about  $0.38 \text{ mm}\cdot\text{s}^{-1}$ ,  $-0.22 \text{ mm}\cdot\text{s}^{-1}$ , and  $51.5 \text{ T}$ , respectively, were attributed to  $\alpha\text{-Fe}_2\text{O}_3$  particles above  $10\text{--}12 \text{ nm}$ . The doublet part in the spectra with  $\delta = 0.35\text{--}0.38 \text{ mm}\cdot\text{s}^{-1}$  and a  $\Delta$  of about  $0.9 \text{ mm}\cdot\text{s}^{-1}$  were assigned to superparamagnetic relaxations of  $\text{Fe}^{3+}$  in smaller nanoparticles or  $\text{Fe}^{3+}$  included in the solid solution. The relative part of the doublet component was more than 80% for the samples with an Fe/Ce ratio up to 2:8 and decreased about three times for 7Fe3Ce\_HT(773). The line width of the sextets varied between  $0.30$  and  $0.39 \text{ mm}\cdot\text{s}^{-1}$ . It was larger than the expected one for the distinct hematite phase, which evidenced variations in the environment around the  $\text{Fe}^{3+}$  nuclei.

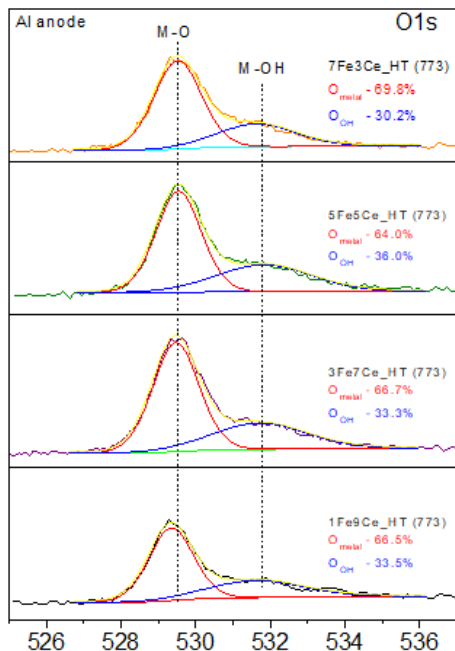


**Figure 6:** O 1s XPS spectra obtained on aluminum anode for selected

X-ray photoelectron spectroscopy (XPS) was performed to characterize the chemical state and the relative proportion of each element on the surface of the binary Fe–Ce oxides with different compositions. The O 1s XPS spectra (Figure 6) represented one main peak centered at  $\sim 529.5 \text{ eV}$ , corresponding to lattice oxygen. The changes in the shape and the position of the main oxygen peak with the Fe/Ce ratio could be assigned to the variations in the oxygen ion environment as the formation of shared Ce–O–Fe bonds and M–OH groups.

The core-level binding energies of Ce (3d) spectra were fitted with five spin-orbit doublets associated with  $\text{Ce}^{3+}$ , and  $\text{Ce}^{4+}$  contributions. The Fe 2p XPS spectra represented two main peaks at  $\sim 710.6$  and  $723.9 \text{ eV}$  corresponding to Fe  $2p_{3/2}$  and Fe  $2p_{1/2}$ , respectively.

XPS data for the surface composition of the samples with different Fe/Ce ratios are listed. It was interesting to note that the surface Fe/Ce ratio did not correspond to the theoretical bulk one (in the table, identified with \*). It was more than twice higher for 1Fe9Ce\_HT(773) with a tendency of a rapid decrease below the theoretical one with the increase of iron content in the samples.

In addition, the small amount of Fe in the samples significantly increased the Ce<sup>3+</sup> content on the surface, while a portion of the reduced ceria ions strongly decreased with the enrichment of the samples with iron. These changes were also accompanied with a significant oxygen deficit (Table 1), which was most pronounced for 1Fe9Ce\_HT(773) and slightly decreased with the increase of the Fe/Ce ratio in the solids.

**Table 1.** Surface composition of selected samples with the variation of Fe/Ce ratio, elucidated by XPS analyses.

Sample	O at%	Fe at%	Ce at%	Ce <sup>3+</sup> at%	Ce <sup>4+</sup> at%	Fe/Ce	O/(Fe+Ce)	Ce <sup>3+/Fe<sup>3+</sup></sup>
CeO <sub>2</sub> _HT(773)	79.5	-	20.5	22.6	77.4	-	3.89	
1Fe9Ce_HT(773)	59.4	8.2	32.4	34.3	65.7	0.25 (0.11*)	1.29	1.35
3Fe7Ce_HT(773)	60.2	9.0	30.8	32.8	67.2	0.30 (0.43)	1.51	1.12
5Fe5Ce_HT(773)	63.1	11.7	25.2	27.7	72.3	0.46 (1.00)	1.71	0.60
7Fe3Ce_HT(773)	65.5	17.1	17.4	28.5	71.5	0.98 (2.33)	1.90	0.29

### 1.2. Catalytic results of mixed metal oxides in Fe-Ce, in the methanol decomposition reaction (MD).

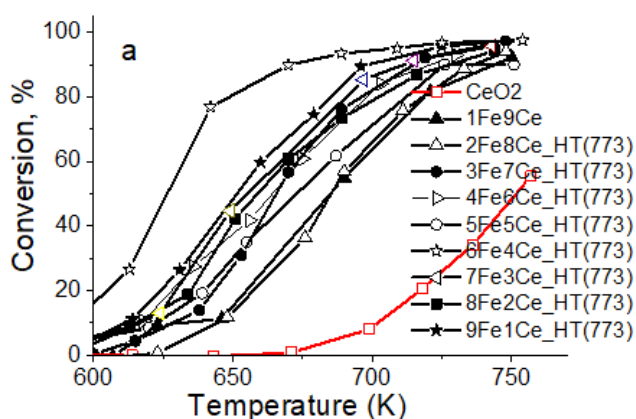


**Figure 7:** Conversion vs temperature in methanol decomposition for ceria-iron oxides with different composition.

In Figure 7, the catalytic behavior of the composites in methanol decomposition is illustrated. The conversion curves for all binary materials were about 100 K shifted to lower temperatures as compared to pure CeO<sub>2</sub>, which undoubtedly evidenced the beneficial effect of iron doping on the catalytic activity. In addition, doping ceria with iron decreased the

ability to methane formation and significantly improved the selectivity to CO (Table 2). CO<sub>2</sub> was also observed as a byproduct for all Fe-containing composites, and its selectivity increased up to 12–15% for the samples with a relatively high Fe/Ce ratio. The sample 1Fe9Ce\_HT(773) exhibited the highest selectivity in methanol decomposition to CO. The increase in the Fe/Ce ratio provided a non-regular increase in the catalytic activity. The highest activity, combined with relatively high selectivity to methane, was registered for 6Fe4Ce\_HT(773). The increase in the basicity of the O ions in the dominant Fe–O–Fe structures facilitates the scission of the H<sub>3</sub>C–OH bond in the methanol molecule, which provided an increase in the methane selectivity.

**Table 2:** Products distribution at 50% conversion of methanol for ceria-iron oxides with variation of Fe/Ce ratio and preparation conditions used of selected samples.

Sample	CH <sub>4</sub>	CO <sub>2</sub>	CO
CeO <sub>2</sub> _HT(773)	79	0	21
1Fe9Ce_HT(773)	24	3	73
3Fe7Ce_HT(773)	45	10	45
5Fe5Ce_HT(773)	47	12	41
7Fe3Ce_HT(773)	44	14	42
9Fe1Ce_HT(773)	41	14	45
3Fe7Ce_HT(573)	57	14	29
3Fe7Ce_Et(773)	52	9	39
3Fe7Ce_Extra(773)	63	11	26
3Fe7Ce_U(773)	31	7	62

## **2. Nickel-Decorated Mesoporous Iron–Cerium Mixed Oxides: Microstructure and Catalytic Activity in Methanol Decomposition.**

### *2.1. Methods of preparation and physicochemical characterization of Ni-Fe-Ce oxides.*

The Fe-Ce mesoporous oxide supports were subjected to preliminary dried at 433 K for two hours. Simultaneously, a 1 mL solution with appropriate concentration of Ni(NO<sub>3</sub>)<sub>2</sub> · 6H<sub>2</sub>O (0.74M) was prepared. The catalytic support was placed in a mortar and quickly soaked with the previously prepared Ni solution. The mixture was left to dry for one day at room temperatures in a dryer. It was then collected from the mortar and calcined at 773 K inside a

muffle. The catalysts thus synthesized have been named: Ni/xFeyCe\_ox; NixFeyCe\_ox where x and y is the molar ration of iron and cerium respectively, the theoretical content of nickel is 8% wt. (the thesis also reports similar nomenclatures relating to various calcination procedures).

The XRD patterns of the as-synthesized Ni/ FeCe composites are presented in Figure 8. The reflections at 28.5, 33.1, 47.5, 56.3, 76.7, and 79.1° correspond to the cubic fluorite-type structure of cerianite (JCPDS 34-0394). The broader reflections in the patterns of the iron-containing samples indicate a higher dispersion of ceria in them (Table 2). The appearance of additional reflections at 24.1, 33.1, 35.6, 40.1, 49.4, 54.0, 62.3, and 63.9° is associated

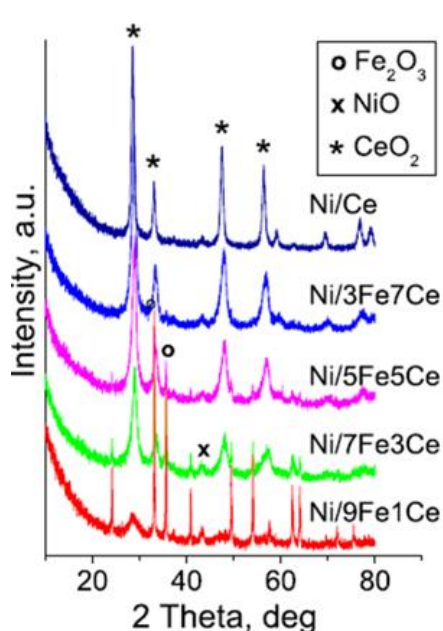


**Figure 8.** XRD patterns of Ni-decorated FeCe supports.

with the coexistence of a rhombohedral hematite phase. The intensity of these reflections sharply increased with the increase in iron content in the samples, which evidences facile segregation of larger hematite particles.

The presence of a larger portion of the hematite phase combined with a lower distortion of ceria and the hematite lattice in their Ni containing analogues indicates that the process of Ni decoration partially decomposes the shared Fe–O–Ce bonds. The observed additional small reflections at 37.3, 43.4, and 63.1°

could be attributed to finely dispersed NiO (JCPDS 89-7131). The EDS images showed that Ni particles

were spread all over the FeCe support, but it seems that they were preferably located in the vicinity of ceria-iron interface (Figure 9).

The room-temperature Mössbauer spectra represented a superimposition of sextets and doublets. The sextet components with an isomer shift of 0.37–0.39 mm s<sup>-1</sup> and a hyperfine field of about 51 T are attributed to  $\alpha$ -Fe<sub>2</sub>O<sub>3</sub>, with an average crystallite size of above 10–12 nm. The variations in the relative part of these components indicate that the segregation

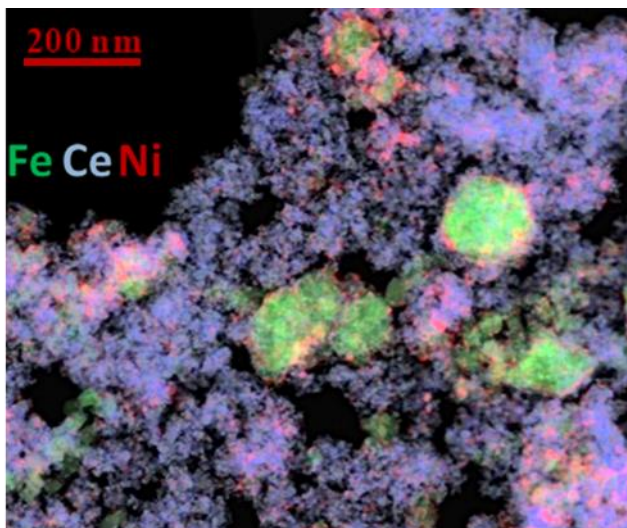


**Figure 9:** EDS images of Ni<sub>5</sub>Fe<sub>5</sub>Ce<sub>773</sub>

of hematite was facilitated by the increase of

the iron content in the samples as well as by the calcination of the supports at higher temperatures. The increase of the sextet components after the decoration with Ni evidences additional segregation of the hematite phase during the modification procedure. The background FTIR spectra of the selected activated composites are shown in Figure 10. The bands at ca. 3730 and 3640 cm<sup>-1</sup> are assigned to hydroxyl groups, likely of Fe–OH and Ce–OH types respectively. The spectra indicate

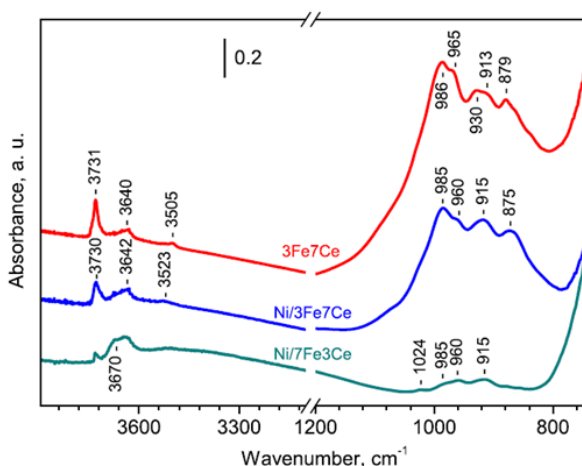


**Figure 10.** Background FTIR spectra of activated 3Fe<sub>7</sub>Ce, Ni/3Fe<sub>7</sub>Ce, and Ni/7Fe<sub>3</sub>Ce.

that during the impregnation procedure, Ni<sup>2+</sup> ions interact predominantly with the 3730 cm<sup>-1</sup> hydroxyl groups because this band appears with a strongly reduced intensity in the spectrum of the nickel containing material. Of course, although weaker, the interaction of the Ni ions with the bridging hydroxyls as well as with the basic oxygen anions of ceria- and hematite-like structures could not be fully ignored.

The IR probe molecules are widely used to characterize different surface sites. The choice of a good probe is essential for obtaining correct information. To assess cationic sites, NO and CO are often used. NO forms nitrosyl with transitional metal cations such as Fe<sup>2+</sup> and Ni<sup>2+</sup> but not with Ce<sup>3+</sup> and Ce<sup>4+</sup>, which allows selective detection of Fe<sup>2+</sup> and Ni<sup>2+</sup> on our samples. Room-temperature adsorption of NO on activated 3Fe<sub>7</sub>Ce<sub>773</sub> led to the

appearance of a strong band at  $1819\text{ cm}^{-1}$  with a low-frequency shoulder at  $1732\text{ cm}^{-1}$  (Figure 11), which is assigned to  $\text{Fe}^{2+}\text{-NO}$  species. The observation of  $\text{Fe}^{2+}$  is due to autoreduction of  $\text{Fe}^{3+}$  upon thermo-vacuum treatment. The high intensity of the bands corresponding to surface nitrosyl groups indicates the presence of a significant amount of coordinatively unsaturated iron ions. When NO was adsorbed at room temperature on the Ni/7FeCe\_773 sample, the intensity of the  $\text{Fe}^{2+}\text{-NO}$

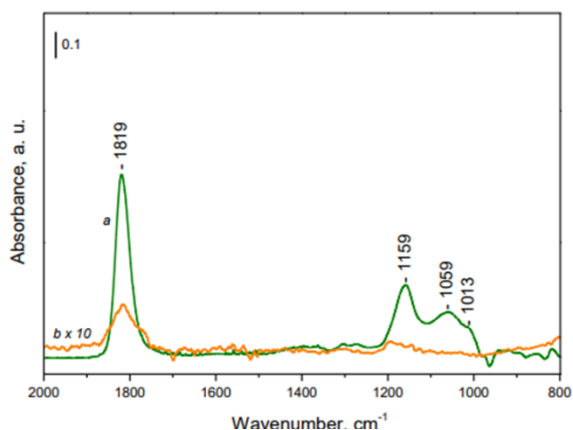


**Figure 11.** FTIR spectra of NO (5 mbar equilibrium pressure) adsorbed at room temperature on 3Fe7Ce (a) and Ni/7Fe3Ce (b).

band at  $1819\text{ cm}^{-1}$  was strongly reduced. This agreed with the observed formation of large hematite particles where the number of iron cations located on the surface was very low. The FTIR spectra of CO adsorbed at 100 K on 3Fe7Ce\_773 and Ni/3Fe7Ce\_773 are very similar (Figure 12).

Two bands, at  $2177\text{--}2176$  and  $2158\text{ cm}^{-1}$ , dominate in the carbonyl region at high coverage. Evacuation at 100 K leads to a fast decrease in the intensity of the band at  $2158\text{ cm}^{-1}$ , which leads to unveiling of another band at ca.  $2169\text{ cm}^{-1}$ .

This band also decreases during evacuation, followed by the band at  $2177\text{ cm}^{-1}$ . After prolonged evacuation at 100 K, weak carbonyl bands remain in the  $2190\text{--}2175\text{ cm}^{-1}$  region. The bands at  $2177$  and  $2169\text{ cm}^{-1}$  are assigned to  $\text{Ce}^{4+}\text{-CO}$  complexes. The band at  $2158\text{ cm}^{-1}$  is due to the presence of H-bonded CO. As was proposed, the lattice charge balance in the binary supports, which appears due to the isomorphous substitution of  $\text{Ce}^{4+}$  ions by lower-

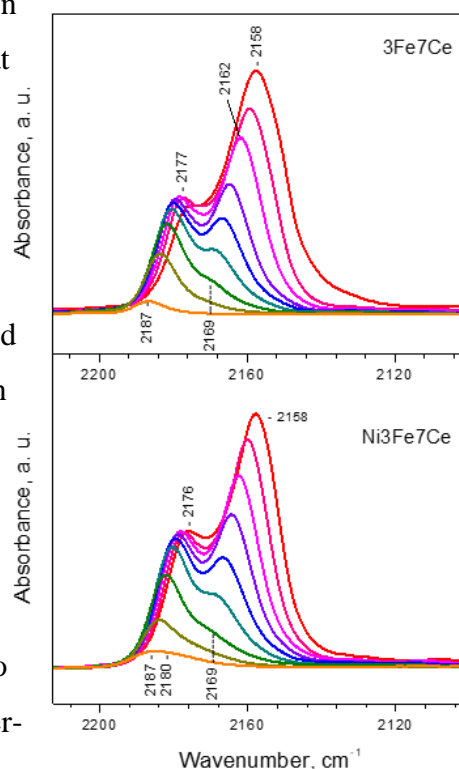


**Figure 12.** FTIR spectra of adsorbed at 100 K CO on 3Fe7Ce and Ni3Fe7Ce at different coverage.

valence  $\text{Fe}^{3+}$  ions, is compensated by the formation of oxygen vacancies and surface hydroxyl groups.

The observed red shift of the  $\nu(\text{OH})$  band at  $3730\text{ cm}^{-1}$  after CO adsorption by 100–160

$\text{cm}^{-1}$  evidences relatively high acidity of the respective hydroxyl groups. This high acidity explains the above-made observation that during the impregnation procedure,  $\text{Ni}^{2+}$  ions interact predominantly with the  $3730\text{ cm}^{-1}$  hydroxyl groups.

## 2.2. In Situ FTIR Mechanistic Studies of Methanol Decomposition.

All spectra were registered after preliminary evacuation of the sample at 723 K (523 K for the first spectrum). For the activated samples, the appearance of terminal ( $\nu(\text{OC})$  at  $1107\text{ cm}^{-1}$ ) and bridging ( $1060\text{--}1030\text{ cm}^{-1}$ ) methoxy groups was established (Figure 13). After the first cycle, transformation of the terminal and partially of bridging methoxy groups to new bridging species monitored at  $1075\text{--}1070\text{ cm}^{-1}$  was observed. A similar effect was described for  $\text{CeO}_2$  and was attributed to the formation of (sub)surface oxygen vacancies. A decrease in the intensity of  $\nu(\text{OC})$  was observed with the rise of the interaction temperature and is related to the change in the surface state under the reaction medium. The effect is weak with the 3Fe7Ce support (Figure 13-A) but is enhanced after decoration with nickel (Figure 13-B). With the iron rich Ni/7Fe3Ce catalysts, no methoxy species were practically observed with the samples treated with methanol at 673 K and above (Figure 13-C). This indicates a decrease in the active oxide surface due to reduction. To obtain information of the eventual intermediate species, spectra were recorded after the interaction with methanol at different temperatures and cooling down in the presence of the gas phase (Figure 14).

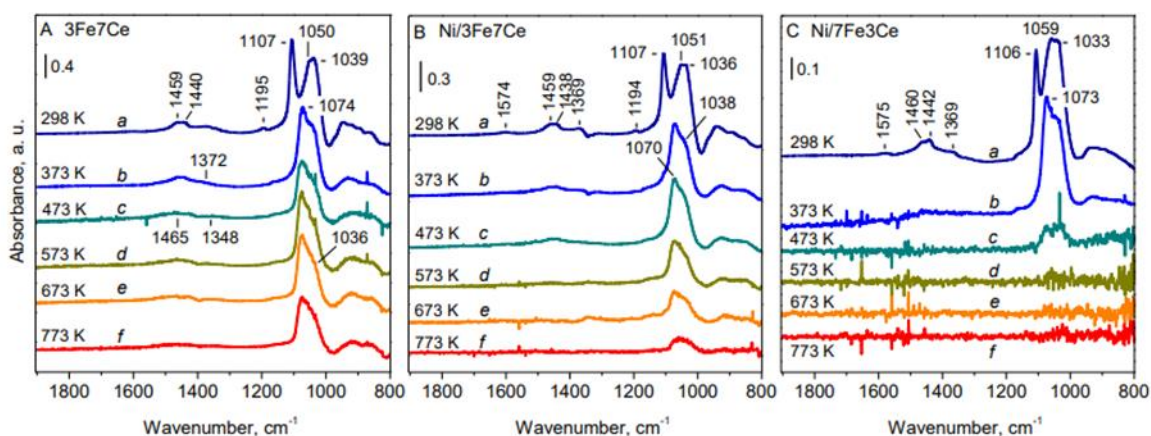


**Figure 13:** FTIR spectra of methanol (10 mbar equilibrium pressure) adsorbed at room temperature on 3Fe7Ce (panel A), Ni/3Fe7Ce (panel B) and Ni/7Fe3Ce (panel C). Spectra a: samples heated in methanol at 373 K followed by cooling to RT; Spectra b-e: samples heated in methanol at the noted temperatures, followed by cooling to RT. The sequence of the spectra recording is from up to bottom.

The treatment with methanol at the 373–473 K range resulted in the appearance of formats (bands at ca.  $1590\text{--}1574$ ,  $1372$ , and  $1332\text{ cm}^{-1}$ ), which, with the temperature increase, were



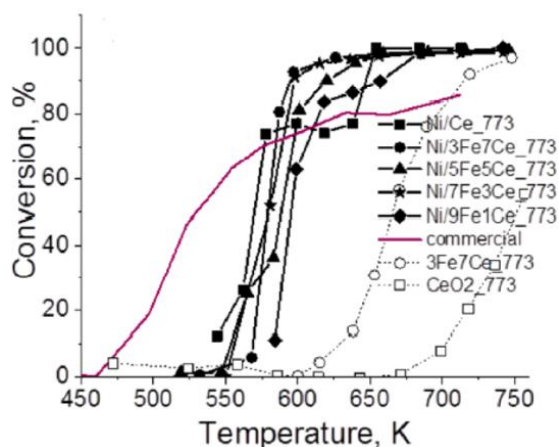


**Figure 15.** Temperature dependence of methanol decomposition on Ni-decorated samples with different compositions. Selected supports and a Cu-containing commercial catalyst are presented for comparison

The temperature dependencies of methanol conversion on Ni-modified iron and cerium oxides are shown in Figure 15. All materials exhibited a strong increase of the catalytic activity above 550 K, and for most of them, about 100% conversion was achieved even below 600 K. The conversion curves of all Ni modifications were steeper and significantly shifted to lower temperatures as compared to the corresponding ceria–iron oxide supports (Figure 15), which well demonstrated the promotion effect of nickel decoration on the catalytic activity.

In addition, Ni-containing materials exhibited above 80–90% selectivity to CO (Figure 16). The H<sub>2</sub>/CO ratio was close to 2 and CO<sub>2</sub> (up to 10–15%), and negligible amounts of methane (up to 2–3%) were also detected as byproducts. For comparison, about 80 and 45% methane were registered for the reference CeO<sub>2</sub> and 3Fe7Ce supports, respectively.

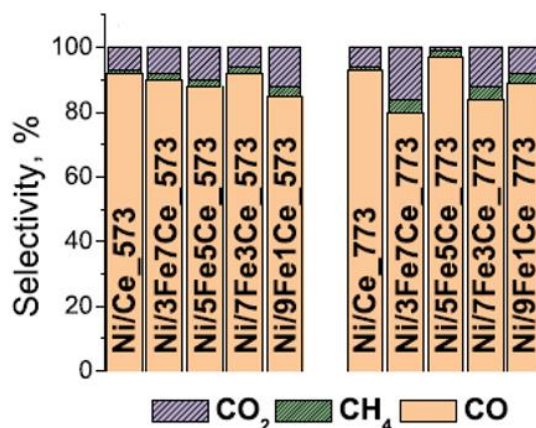
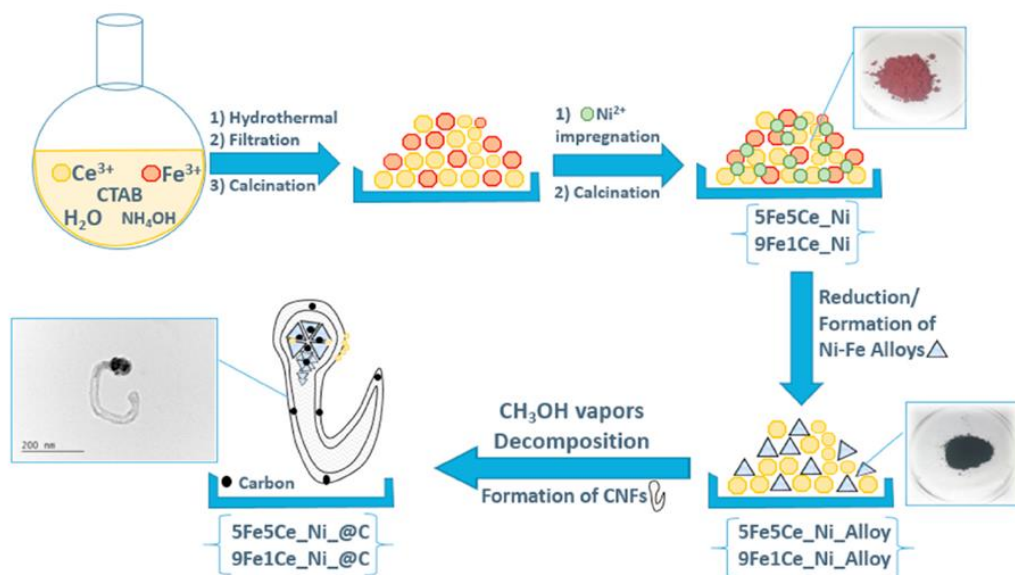


**Figure 16:** Products' distribution at 50% conversion.

### **3. Mesoporous Ce–Fe–Ni nanocomposites encapsulated in carbon-nanofibers catalytic behavior in oxygen evolution reaction.**

#### ***3.1. Methods of preparation and physicochemical characterization.***



**Scheme 1:** Schematic illustration of the synthetic procedure adopted for the synthesis and encapsulation of the catalysts within CNFs, and related nomenclature of catalysts.

XRD patterns of the initial Ni–Fe–Ce oxides and their modifications are shown in Figure 17.

The crystalline phases obtained for the mixed metal oxides of Fe-Ce-Ni, include cerianite, hematite and bunsenite, as discussed in the previous chapters.

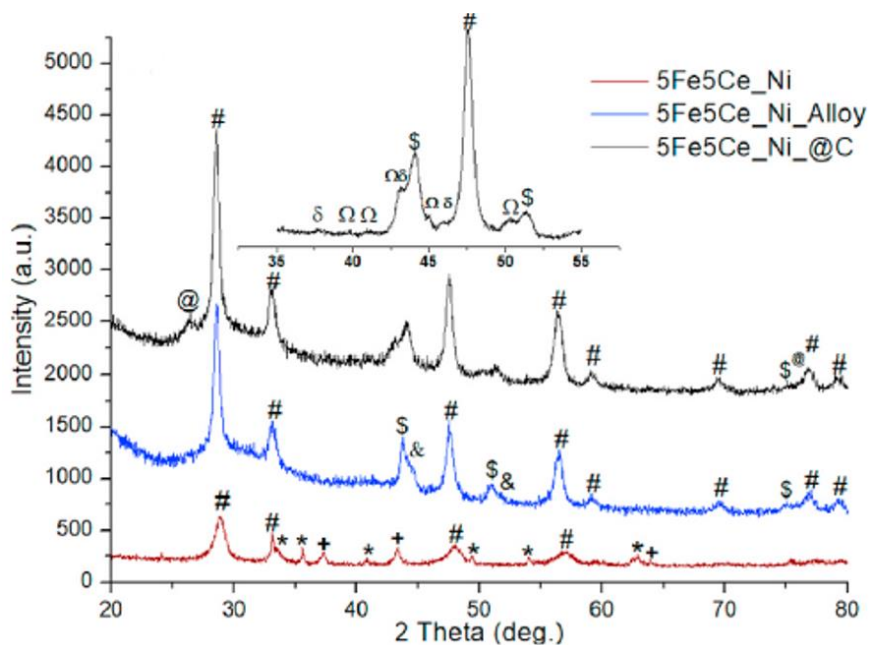


**Figure 17:** XRD patterns of 5Fe5Ce\_Ni –based materials, the correspondence of the peaks is indexed as follows: (#) CeO<sub>2</sub>, (\*) Fe<sub>2</sub>O<sub>3</sub>, (+) NiO, (\$) (Ni,Fe)-Alloy, (&) Ni, (@) Graphite-2H, (δ) Fe<sub>3</sub>C, (Ω) Fe<sub>5</sub>C<sub>2</sub>. Inset: magnification of the 2θ range between 35° and 55°.

After the treatment in hydrogen atmosphere (Figures 17, sample 5Fe5Ce\_Ni\_Alloy), the reflections of cerianite are still distinguished. The observed slight increase in the ceria unit cell parameters after the reduction could be due to the release of the incorporated in the ceria lattice iron ions and generation of additional oxygen vacancies in it. The reduction transformations of the parent mixed oxides are also confirmed with the appearance of additional reflections at  $2\theta = 43.7^\circ, 50.8^\circ, 74.6^\circ$  and  $2\theta = 44.5^\circ, 51.6^\circ, 76.3^\circ$  typical of Ni-Fe alloys (JCPDS 38-0419) and metallic Ni (JCPDS 01-071-4655), respectively. Generally, the crystallite size of the metal phases is below 35 nm indicating that ceria hinders their agglomeration. The carbon coating process, carried out on the reduced catalysts (Figures 17 in black), leads to the appearance of reflections at  $2\theta = 37.8^\circ, 39.8^\circ, 40.7^\circ, 42.8^\circ, 45^\circ$  and  $46^\circ$  (in the short angle magnification in Figure 17) of  $\text{FeC}_3$  (JCPDS 35-0772) and reflections at  $2\theta = 40.9^\circ, 43.3^\circ, 44.2^\circ, 45^\circ, 46.5^\circ, 50^\circ, 50.3^\circ$ , attributable to  $\text{Fe}_5\text{C}_2$  (JCPDS 51-0997). The carbides are in coexistence with NiFe alloy and  $\text{Ni}^0$  nanoparticles, while the reflection at  $2\theta = 26.5^\circ$  in both samples (5Fe5Ce\_Ni\_@C and 9Fe1Ce\_Ni\_@C) are associated with the (002) plane of graphite-2H (JCPDS 41-1487).

In order to assess the textural changes in the specimens under investigation,  $\text{N}_2$ -physisorption measurements were carried out. The absorption-desorption curves, shown in, can be classified as type IV-a isotherms, typical of mesoporous solids, for both catalyst series (5Fe5Ce\_Ni-based and 9Fe1Ce\_Ni-based). The hysteresis loop, on the other hand, can be classified as type H3. The absence of sharp step-downs in the desorption curve suggests a cylinder-like pores with shrinkage-free pore-necks. The growth of the carbon nanofibers around the nanoparticles after the treatment in methanol causes a predictable increase in the specific surface area of the samples. The significantly higher SBET for 5Fe5Ce\_Ni\_@C as compared to 9Fe1Ce\_Ni\_@C it may be due to a greater growth of the carbon component, combined with the development of a significant portion of micropores.

**Table 3:** BET surface area (SBET), micropores specific surface area ( $S_{\text{micro}}$ ), total pore volume ( $V_{\text{tot}}$ ) and average pore diameter ( $D_{\text{pores}}$ ) of 5Fe5Ce\_Ni based and 9Fe1Ce\_Ni based materials.

Sample	$S_{\text{BET}}$ ( $\text{m}^2/\text{g}$ )	$V_{\text{tot}}$ ( $\text{cc}/\text{g}$ )	$D_{\text{pores}}$ (nm)	$S_{\text{micro}}$ ( $\text{m}^2/\text{g}$ )
5Fe5Ce_Ni	60	0.25	10.6	–
5Fe5Ce_Ni_Alloy	57	0.24	6.6	–
5Fe5Ce_Ni_@C	154	0.77	3.8	16
9Fe1Ce_Ni	32	0.18	13.3	–
9Fe1Ce_Ni_Alloy	41	0.22	13.5	–
9Fe1Ce_Ni_@C	84	0.33	3.8	0.8

The high resolution images in Figure 18-C clarify the layering and presence of the distorted crystallographic planes of graphite-2H (3.1 Å - 3.34 Å), values confirmed for the samples by the SAED patterns shown in Figure 18-E. The Figure 18-D shows d-spacing of about 2.7 Å, coming from particles adhered to the outer wall of the nanofiber, and attributable to the (200) plane of CeO<sub>2</sub>, which evidently does not seem to take an active part in the growth process of the fibers.

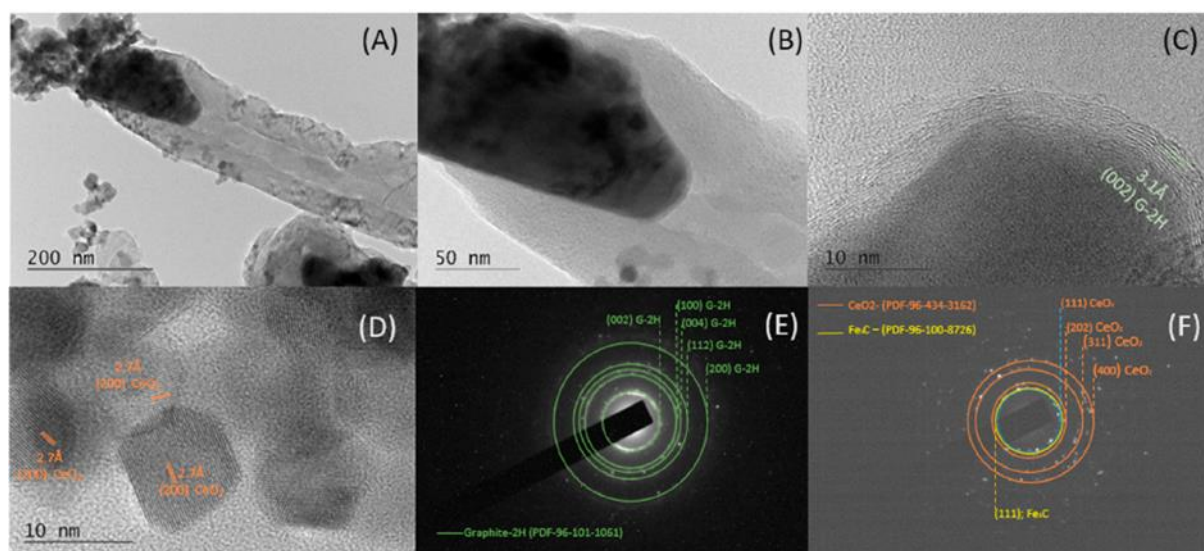


**Figure 18:** TEM images of the sample 5Fe5Ce\_Ni\_@C. (a) 40k of magnification. (b) 100k of magnification. (c) 600k magnification first spot. (d) 600k magnification second spot. (e) SAED first spot. (f) SAED second spot.

The carbon nanofibers (CNFs) in Fig. 18-A, can be classified, with the nomenclature "bamboo-like" CNFs or "stacked-cups"-CNFs, due to the characteristic bamboo structure of the trunk of the fiber. The mechanism proposed for the growth of CNFs can be factored into three main phases: (I) the decomposition of the organic molecule on the active metal surface, (II) diffusion of carbon inside the metal particle, and formation of thermodynamically more stable carbides, (III) layering of graphite and encapsulation of the nanoparticle with the formation of a "carbonaceous restriction" which will act as a nucleation point for the subsequent growth of the nanotube until the formation of a new nucleation point and subsequent formation of a second segment.

### 3.2. Catalytic activity in electrolytic splitting of water - half-reaction of Oxygen Evolution Reaction in an alkaline environment.

The linear sweep voltammograms of the 5Fe5Ce\_Ni-based samples conducted at room temperature in a deaerated 1 M KOH aqueous solution are shown in Figure 19. Based on the curves shown, it can be easily noticed that the reduction treatment and the subsequent

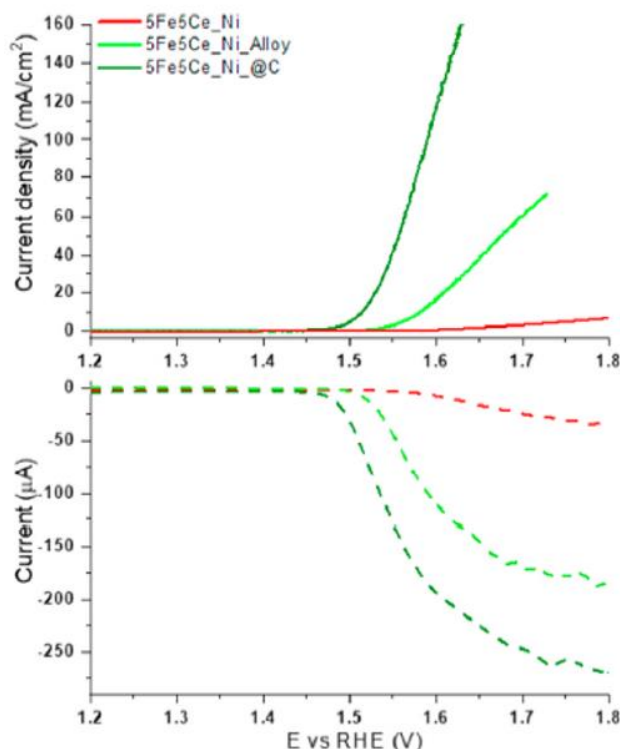


**Figure 19:** Linear sweep voltammetry at 5 mV/s, 1800 rpm in 1 M KOH for 5Fe5Ce\_Ni-based materials.

encapsulation inside the carbon nanofibers of the mixed metal oxides, considerably increased the current density ( $j$ ), produced during the OER reducing the overpotential ( $\eta$ ) required to perform it. The linear sweep voltammetric curves showed first of all the poor activity of the catalysts composed of mixed metal oxides with a current density less than 10 mA/cm<sup>2</sup> at 1.8 V vs. RHE (overpotential of 570 mV). The reduction treatment and consequent formation of metallic species inside the catalysts visibly improved the activity towards the OER reaction, leading the samples 5Fe5Ce\_Ni\_Alloy present an overpotential at 10 mA/cm<sup>2</sup> corresponding to 340 mV. The

performance of both series of catalysts took a qualitative leap forward after the partial transformation of the metal species into carbides and their subsequent encapsulation within the carbon nanofibers. In fact, the 5Fe5Ce\_Ni\_@C sample shows (at the same quantity of catalyst grafted onto the RRDE as the previous ones) an overpotential of 280 mV at 10 mA/cm<sup>2</sup>. CNFs-containing catalysts, under the same or similar operating conditions, show lower or at least competitive values of overpotential, compared to IrO<sub>2</sub> or Ir-based catalysts commercially in use for OER in alkaline environment. (e.g. IrO<sub>2</sub> with  $\eta$  = 281 mV).

### 3.3. Electrochemical Impedance Spectroscopy (EIS).

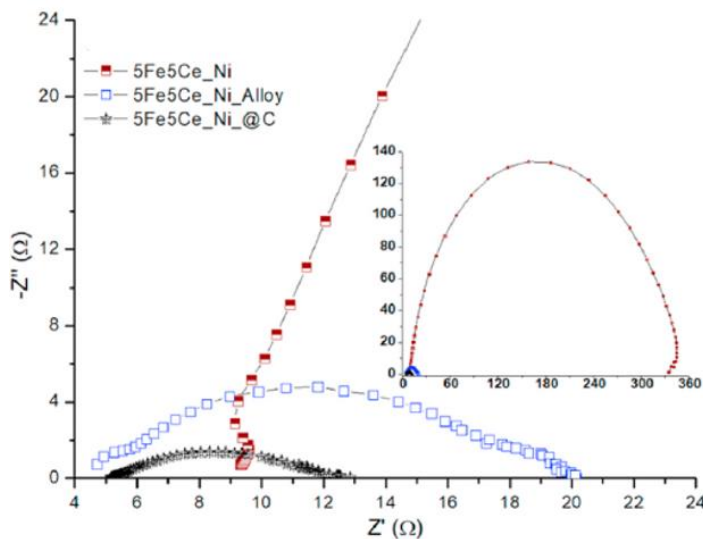


**Figure 20:** Nyquist plots of 5Fe5Ce\_Ni-based catalysts, carried out at 1.6 V vs RHE with 10 mV of amplitude (r.m.s.). The inset is the overview.

The overlapped Nyquist plots are shown in Figure 20. A full semi-circular loop was observed for each study case, the samples 5Fe5Ce\_Ni, have a total polarization resistance ( $R_p$ ), of 338  $\Omega$ , respectively. Such high values are usually considered proportional to an equally high charge transfer resistance by the catalysts. The reduced homologous catalyst show a huge decrease in  $R_p$  equal to 14.2  $\Omega$ , this may be due to a fine dispersion of Ni metal

nanoparticles and Ni–Fe alloys within the  $\text{CeO}_2$  which is reflected in a more efficient synergistic action in the charge transfer process. In the CNF-based catalysts, the sample 5Fe5Ce\_Ni\_@C, shows an  $R_p$  equal to 7.8  $\Omega$ . The shown lower increase in the imaginary component of the impedance ( $-Z''$ ) together with a semi-circle of smaller diameter in the low frequency zone, are an evidence of the improvement of charge- and electron-transfer properties and of the capacitive characteristics of CNFs compared to their respective precursors.

### 3.4. Cyclic voltammetry (CV), Electrochemically active surface area (EASA).

Cyclic voltammetry studies have been carried out for the assynthesized composites, at first in the potential range between 0.05 and 1.15 V vs. RHE at the scan rate of 0.02 V/s. Figure 21 shows the voltammograms of the catalysts under examination at room temperature in a de-aerated solution of 1 M KOH. The non "rectangular" shape of the voltammograms indicates an important contribution of the pseudocapacitive nature of the process within the aforementioned potential range, from which, however, it can be appreciated the difference in absolute area under the CV curves (AUC), that follows positive growth following the order: Mixed Metal oxides < Reduced-Metal oxides  $\ll$  CNFs.

As it is possible to notice, the trend of capacity growth is quite similar to the trend of anodic growth in the OER reaction (Figure 19), leading to the conclusion that, the increase in current density followed by a lowering of the overpotential is related not only to a progressive improvement of the intrinsic mechanism of charge transfer of the catalysts (as seen from the EIS analysis in Figure 20), but also due to an increase in the following characteristics:

- 1) electrocatalytically active surface accessible (ECSA);
- 2) the active sites immediately present at the electrolyte-electrode interface;
- 3) possible active sites formed by activation processes that occur in the activation of carbon edges when increasing potentials.

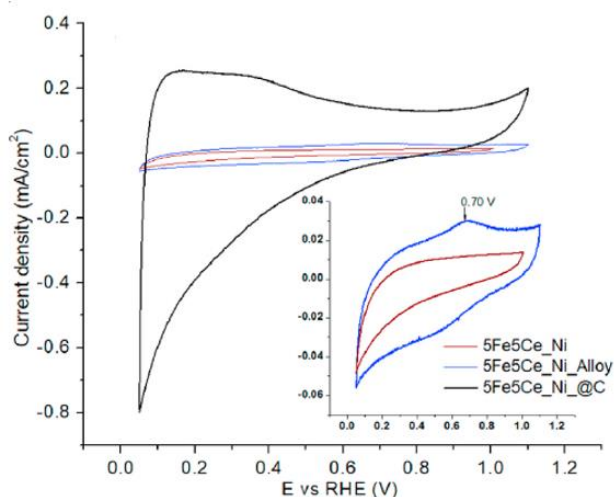


**Figure 21:** Cyclovoltammetric profiles of 5Fe5Ce\_Ni-based materials materials, in the potential range between 0.05 and 1.15 V vs. RHE at the scan rate of 0.02 V/s inset: enlargement of the CV profiles of 5Fe5Ce\_Ni and 5Fe5Ce\_Ni\_Alloy.

**Table 4:** Electro-kinetic parameters for OER including: the overpotential ( $\eta$ ),  $iR$ -corrected, at 10 and comparison between active surfaces ( $m^2/g$ ).

Sample	BET-SA ( $m^2/g$ )	ECSA ( $m^2/g$ )	$\eta$ $iR$ -free, $j=10 \text{ mA/cm}^2$ (mV)
5Fe5Ce_Ni	60.13	–	>570
9Fe1Ce_Ni	32.1	–	450
5Fe5Ce_Ni_Alloy	57.3	0.65	340
9Fe1Ce_Ni_Alloy	41.6	0.49	390
5Fe5Ce_Ni_@C	154.4	7.27	280
9Fe1Ce_Ni_@C	84	9.21	280

#### 4. Ni-Sn alloys supported on CeO<sub>2</sub>/Ce(Zr)O<sub>2</sub>: catalytic behavior in the aqueous phase reforming of ethylene glycol (EG) in a variable reaction environment.

##### 4.1. Methods of preparation and physicochemical characterization.

For the reaction of APR-EG<sub>6%</sub>, three main catalysts were prepared at different weight percentages of tin but at the same theoretical weight percentage of nickel. For this purpose, different weight percentages of tin (2.5% wt., 5% wt. and 10% wt.) and 10% wt. by weight of nickel were added to 2g of CeO<sub>2</sub>/Ce(Zr)O<sub>2</sub> support. In order to promote the formation of Ni-Sn alloys, the three mixed metal oxide catalysts were subjected to a hydrogen reduction procedure inside of a continuous flow reactor. Table 5 lists the catalysts pre and post reduction process and their reference monometallic counterparts.

**Table 5:** Ni-Sn modified Ce-Zr oxide supports and the respective monometallic references.

Sample	Sn content, % wt.	Ni content, % wt.	Treatment medium
2.510SnNi-CZ	2.5	10	Static air
510SnNi-CZ	5	10	Static air
1010SnNi-CZ	10	10	Static air
2.510SnNi-CZ_red	2.5	10	hydrogen
510SnNi-CZ_red	5	10	hydrogen
1010SnNi-CZ_red	10	10	hydrogen
2.5Sn-CZ_red	2.5	-	hydrogen
5Sn-CZ_red	5	-	hydrogen
10Sn-CZ_red	10	-	hydrogen
10Ni-CZ_red	-	10	hydrogen

Typically, 0.5 g of the reduced catalyst was transferred into the reactor containing 6% wt ethylene glycol solution. The mixture was continuously stirred at 400 rpm. The reactor was purged with nitrogen flow and pressurized with an initial pressure of 20 bar which served also as internal standard for the quantification of the gaseous products. The reactor was then heated at 543 K and held at this temperature for 2 h. Finally, the reactor was cooled down to room temperature. The gaseous products were collected in a sampling gas bag and analyzed on a GC. After depressurization, the liquid products were collected and filtered with a 0.25 µm PTFE filter and analyzed on a HPLC and GC-MS. Experiments for all catalysts in the list were carried out twice, starting from "standard" conditions using an initial pH of 7 and then under alkaline conditions, starting from an initial pH of 14.

To better elucidate the relative composition of the species present inside the bimetallic catalysts,  $^{119}\text{Sn}$ -Moessbauer spectroscopy was used. Figure 22 shows the Moessbauer spectra obtained from the three bimetallic samples in their oxidized phase and in their reduced phase.

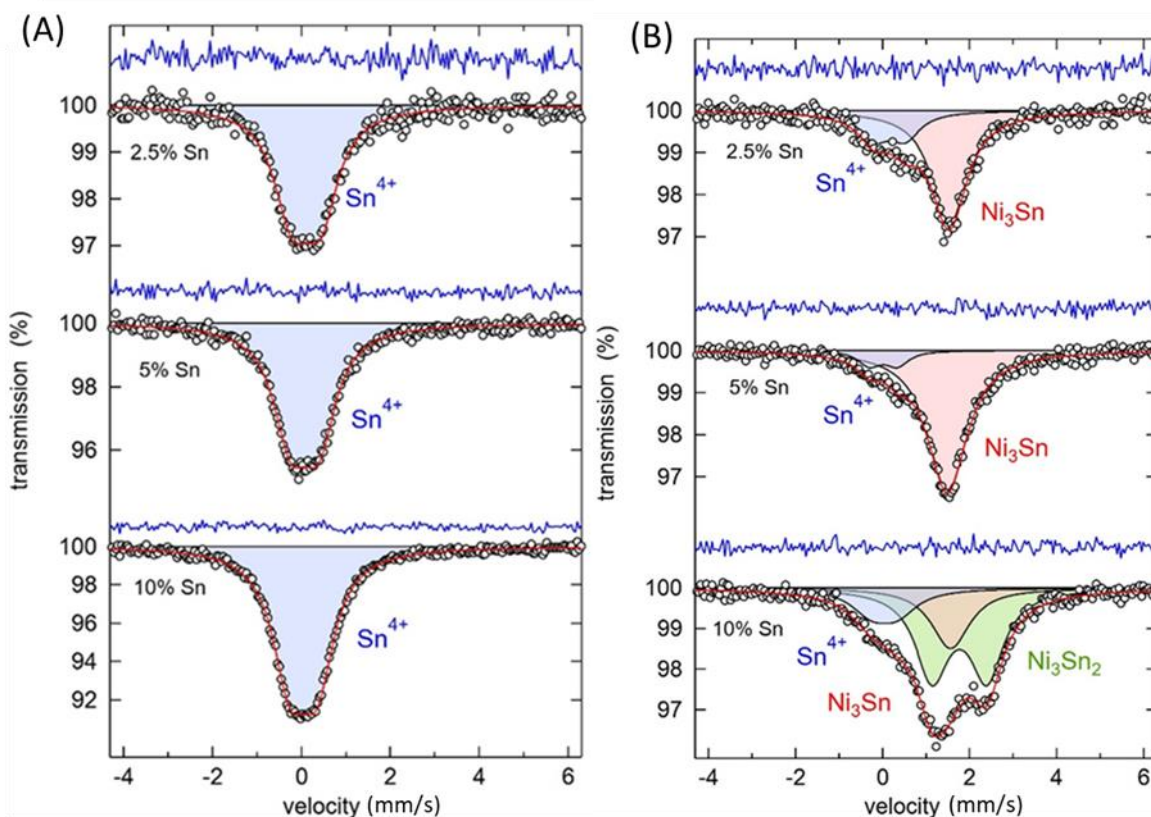


**Figure 22:**  $^{119}\text{Sn}$  Mössbauer spectra of bimetallic NiSn supported on Ce-Zr-oxide for different Sn contents (2.5, 5, and 10%) for fixed Ni content (10%), in their oxidized form (A) and in their reduced form (B).

For the mixed metal oxides (Figure 22-A) only one contribution is visible that can be assigned to  $\text{Sn}^{4+}$ . Probably due to the presence of  $\text{SnO}_2$ . Figure 22-B instead shows a more detailed image (from the nuclear spectroscopic point of view of tin), of the metal-catalytic active phase used at the time of the reaction, therefore after the reduction and activation process of the catalysts. For all samples, multiple contributions are visible in the spectra. For the samples with 2.5% and 5% Sn, the spectra are dominated by a singlet with isomer shift IS close to 1.5 mm/s. This contribution can be assigned to  $\text{Ni}_3\text{Sn}$  particles. A second contribution close to 0 mm/s reveals the presence of some  $\text{Sn}^{4+}$ , possibly in  $\text{SnO}_2$ . For the largest Sn content (10%), the spectrum is dominated by a doublet with IS = 1.8 mm/s and quadrupole splitting QS = 1.2 mm/s, which is characteristic of  $\text{Ni}_3\text{Sn}_2$ . In addition, contributions from  $\text{Ni}_3\text{Sn}$  and  $\text{Sn}^{4+}$  are visible again. The relative abundance of the tin

species present in the samples, with a greater focus on reduced samples, also allows us further clarification. In fact, it is interesting to note, how the sample 2.510SnNi-CZ\_red has a concentration of  $\text{Sn}^{4+}$  almost double compared to the sample 510SnNi-CZ\_red. This  $\text{Sn}^{4+}$  can be distributed inside the support both as a finely dispersed  $\text{SnO}_2$  and as a defective  $\text{Sn}^{4+}$  inside the crystal lattice of the  $\text{Ce}(\text{Zr})\text{O}_2$  support, this would explain why during the reduction process, only a small amount of tin, subjected to the sintering process, led to the formation of the  $\text{Ni}_3\text{Sn}$  alloy. On the other hand, the 1010SnNi-CZ\_red sample containing a greater quantity of tin than its reduced counterparts, also possesses a greater availability and mobility of it during the reduction and sintering process, thus leading to the formation of not only from the  $\text{Ni}_3\text{Sn}$  alloy but also to an alloy with a higher concentration of tin ( $\text{Ni}_3\text{Sn}_2$ ). Also from Figure 22, it can be noted that the presence of  $\text{Sn}^0$  was not detected.

On a macroscopic level, the reduction process does not bring any obvious changes to the textural characteristics of the catalysts. In the TEM images (Figure 23 A-B), it can be seen that the size of the constituent particles of the catalyst remains almost unchanged after the reduction process, with greater inter-particle association for sample 510SnNi-CZ\_red probably due to the sintering and coagulation processes of the smaller particles.

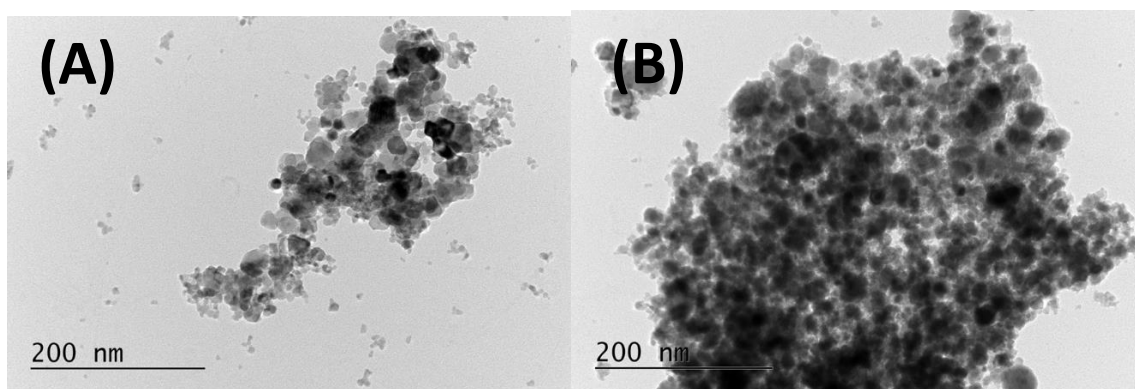


**Figure 23:** HR-TEM images of the selected sample 510SnNi-CZ (A) and 510SnNi-CZ\_red (B) at 40k magnification.

This sintering process inevitably affects the surface characteristics of these porous catalysts. The nitrogen physisorption technique was used to test the textural properties and morphological characteristics of the porous structure of the Ceria-Zirconia support and its catalytic derivatives impregnated with different weight percentages of Nickel and Tin. Table 6 reports the textural parameters obtained from  $\text{N}_2$ -physisorption, confirming what was hypothesized by the observation of the HR-TEM images (Figure 23 A-B). In fact, it can be seen how the surface area of the support, originally equal to  $105 \text{ m}^2/\text{g}$ , is considerably

reduced first following the doping in Ni-Sn and subsequently after the reduction process, also the 510SnNi\_CZ catalyst, which had maintained a good area superficial, undergoes a drastic structural decrease due to interparticle coagulation.

**Table 6:** BET surface area, total pore volume ( $V_{tot}$ ) and average pore diameter ( $D_{pores}$ ) of SnNi-based materials in their oxidized state and of the sample 510SnNi-CZ\_red.

Sample	BET ( $m^2/g$ )	$V_{total}$ (mL/g)	$D_{pores}$ (nm)
CZ-support	105	0.10	4.1
2.510 SnNi-CZ	49	0.11	9.1
510SnNi-CZ	95.1	0.14	6.2
1010SnNi-CZ	56.7	0.10	7
510SnNi-CZ_red	51.3	0.096	7.5

#### 4.2. Catalytic properties in APR of ethylene glycol in a variable reaction environment.

As already defined in detail in paragraph 4.1, the current ethylene glycol (6% wt.) APR experiments (APR-EG) were performed in a batch reactor and under the experimental conditions summarized in Table 7.

**Table 7:** Experimental conditions in the APR-EG reaction in Standard and Alkaline environment.

<b>Initial Pressure [bar]</b>	20
<b>Temperature [°C]</b>	270
<b>Feed Concentration [%wt]</b>	6
<b>Feed</b>	Ethylene Glycol
<b>Agitation [rpm]</b>	500
<b>Catalyst amount</b>	0.5g

The experimental results shown in Figure 24 present several insights into the advantages of using the bimetallic catalyst and the correct choice of reaction environment for a highly selective product yield. The first assessment that can be made concerns the substantial difference in  $H_2$  yield between monometallic and bimetallic catalysts operated under standard conditions and those operated in an alkaline environment. It can therefore be seen that this yield is about ten times higher in an alkaline environment than in a neutral pH feed. It can also be seen in the same figure that under both operating conditions, the monometallic nickel catalyst (10Ni-CZ) exhibits proportionately higher activity than both its monometallic and bimetallic counterparts.

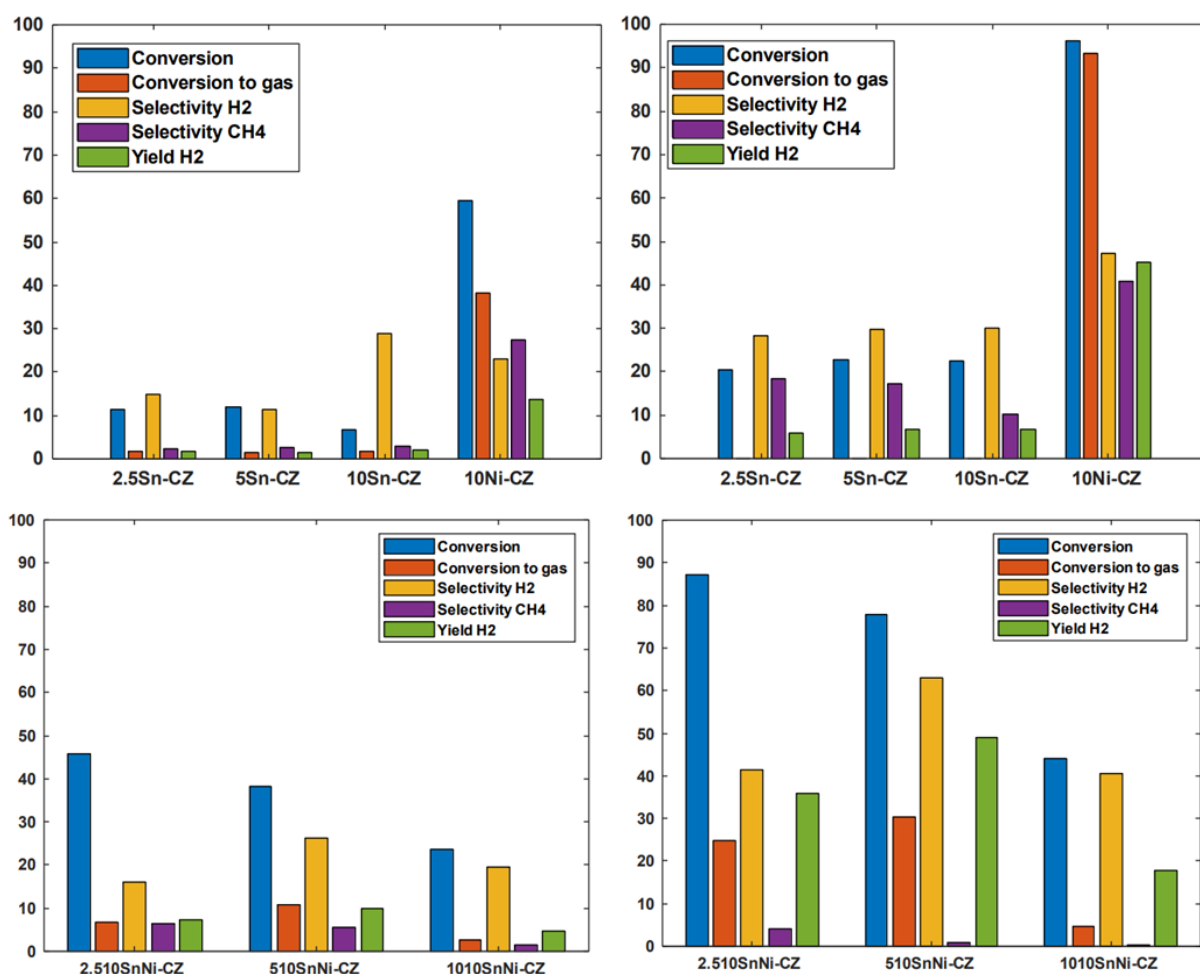


**Figure 24:** Overview results - Aqueous phase reforming of 6%wt EG aqueous solution. For the monometallic references at standard conditions - initial pH=7 (top panel left) at alkaline conditions – initial pH 14 (top panel right); And for bimetallic catalysts at standard conditions - initial pH=7 (bottom panel left) at alkaline conditions – initial pH 14 (bottom panel right).

A higher conversion of ethylene glycol, and even a roughly good hydrogen yield, was expected from the nickel catalyst as it is known to be a metal particularly active in reforming processes, however, its high selectivity for methane production is particularly well known. It is evident from Figure 24 how the use of tin powerfully suppresses the selectivity of nickel for the methanation reaction. A striking example of this behaviour can be observed by focusing on the results obtained from the 10Ni-CZ and 510SnNi-CZ catalysts (both in their reduced state at the time of the reaction) in an alkaline environment (Figure 24 right top and bottom panels). While the conversion of ethylene glycol is over 93% for the 10Ni-CZ catalyst and the selectivity for hydrogen is about 47%, the selectivity for methane is over 55%, resulting in a practically comparable H<sub>2</sub> and CH<sub>4</sub> production. The 510SnNi-CZ catalyst under alkaline conditions has a markedly different productivity,

although the conversion of ethylene glycol is moderately reduced in comparison with its monometallic counterpart (about 78% of EG was converted, Figure 24 lower right panel), its selectivity for hydrogen is slightly higher (55%) but, as shown, the selectivity for the methanation reaction is completely suppressed (selectivity for CH<sub>4</sub> less than 0.9%).

Figure 25 shows the concentration in g/L of the majority products of the liquid phase obtained from the APR reactions.

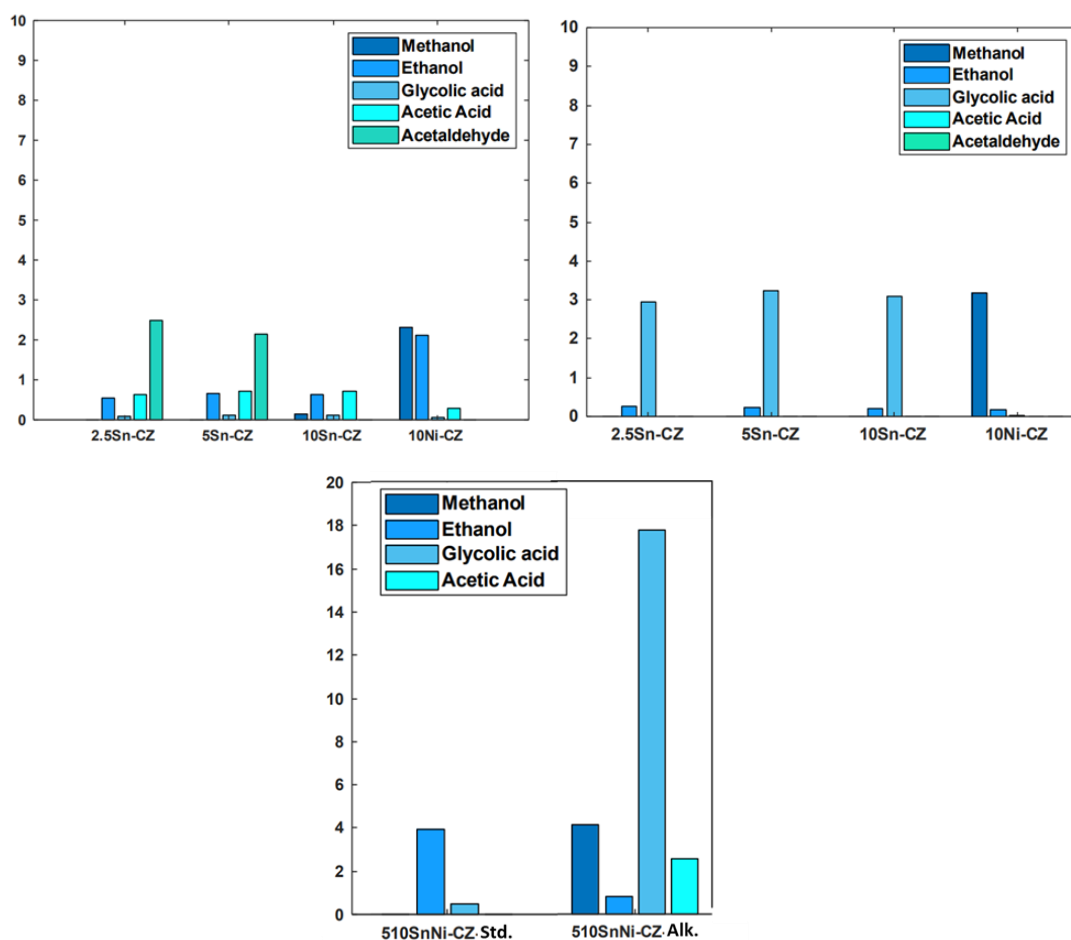


**Figure 25:** Liquid phase concentration [g/L] – Main products present in the liquid phase. At standard conditions - initial pH=7 (top left). At alkaline conditions – initial pH 14 (top right) for the monometallic samples and for a selected bimetallic sample (bottom centered).

Again, it can be seen that monometallic tin catalysts have a particularly different liquid-phase composition than the usual products generally found in the liquid phase after aqueous-phase reforming of ethylene glycol. As can be seen from the 10Ni-CZ catalyst operated under standard conditions, the typical products of this reaction are generally short-chain alcohols, methanol and ethanol, generally produced after fragmentation of the C-C and C-OH bonds of ethylene glycol on the catalyst surface. Under normal operating conditions, it would therefore appear that the reforming reaction on a nickel catalyst presents only a

limited number of feed fragmentation pathways leading to the formation of complex products such as carboxylic acids (in this case acetic acid, Figure 25) and thus the probable carboxylation of a methoxy group. A hypothetical response to this type of behaviour could be found in the results obtained from the gas phase of the 10Ni-CZ catalyst under standard conditions, in fact, the high propensity of this metal for the methanation reaction could inhibit the formation of carbonylated and carboxylated species and thus in this case the formation of acetic acid. Following the same line of logic, monometallic tin catalysts, given their low propensity for methanation reaction, have a marked propensity for the carbonylation reaction of the methoxyl groups present on the catalyst surface and the formation of a good amount of acetaldehyde as the major component. Although of a complex mechanistic nature, the liquid-phase products of reactions in an alkaline environment can be defined as a logical consequence of the above. There are no particular variations as regards the species produced by the 10Ni-CZ catalyst in an alkaline environment, apart from a potent production of methanol as opposed to ethanol, a sign that the fragmentation of the C-C bond of ethylene glycol is preferential in an alkaline environment. The predominant formation of glycolic acid in tin monometallic samples operated under alkaline conditions could be a consequence of acetaldehyde hydroxylation, although the reaction mechanism still needs to be clarified. The bimetallic 510SnNi-CZ sample operated under alkaline conditions, however, shows a combination of the majority product distribution of the two monometallic counterparts, with a marked preference for the fragmentation mechanism operated by tin, with a preponderant formation of glycolic acid (Figure 25, bottom centered).

#### *4.3. Analysis of spent catalysts and possible synergistic contribution of the support in the APR reaction.*

A preliminary study on the recognition of the crystalline phases resulted in the catalysts after the APR-EG processes shows the formation of as many as two different ceria carbonates. Since the only possible carbon sources derive from the reforming process, it is not hazardous to claim that in this case the support acts as a collector of carbonaceous products from the reaction environment. This behavior could in a certain sense favor the reaction, subtracting the reaction products (such as CO) and in a certain way unbalance the reaction balances in favor of a massive production of hydrogen to the detriment of the

methanation reaction. The support would then behave synergistically with the metal active phase in the process, in this case the Ni<sub>3</sub>Sn alloys.

## **CONCLUSIONS:**

- 1) A facile synthesis of nanoscale mesoporous binary cerium–iron oxides in a wide concentration region was demonstrated using a hydrothermal technique and CTAB as a structure-directing agent. These materials represent a complex mixture of differently substituted hematite and ceria phases.
- 2) For the first time, the formation of binary cerium–iron oxides is assumed as different routes in a common mechanism scheme. The formation of shared Ce–O–Fe structures by insertion of Fe<sup>3+</sup> in the ceria lattice is only the first step of the interaction. Under a low Fe/Ce ratio, the compensation of the lattice charge balance is realized predominantly by the formation of bridged OH groups. At a higher Fe/Ce ratio, the facile compensation of the lattice charge balance by the Fe<sup>3+</sup> ions promote the formation of Fe–O–Fe entities within the ceria. The proposed mechanism reveals proper understanding of the relation between the phase composition, texture, and structure features of the binary materials and their catalytic behavior in different redox processes, such as methanol decomposition.
- 3) The binary materials could be considered as highly defect ceria matrix, in which stabilization of isolated Fe<sup>3+</sup> ions and hematite-like structures occur. Their proportion could be effectively controlled by the Fe/Ce ratio and/or preparation conditions used, such as the nature of the solvent, the precipitation agent, the approach of the template release, and the calcination temperature.
- 4) The changes of the Fe/Ce ratio as well as the calcination temperature regulate the formation of Fe<sub>x</sub>Ce<sub>1-x</sub>O<sub>2</sub> solid solution and segregation of ceria and iron oxide structures. Their proportion influences in a complex way the environment and the stabilization of the supported on them NiO entities.
- 5) By grafting of Ni nanoparticles onto mesoporous ceria-iron oxide supports, highly active and stable for operation in wide temperature range catalysts for methanol decomposition could be produced. The superimposition of the effects originated with thermal stability enhancement due to the incorporation of Fe in ceria and increase of redox

ability in presence of Ni improves the catalytic activity of NiFeCe composites at higher temperature. In addition, FeCe supports provide generation of surface methoxy intermediates, the transformation of which is promoted by finely dispersed NiO particles located at the interface between the cerium- and iron containing phases.

6) The catalyst phase composition significantly changes under the reaction medium. This affects the catalytic behavior by: (i) regulation of the amount of defects in the ceria-iron oxide interface, (ii) stabilization of small Ni particles by “encapsulation” in carbon filaments and (iii) changes in the reaction mechanism due to phase transformations leading to the formation of metal carbides and alloys.

7) The metal oxides of iron and nickel within  $\text{CeO}_2$ , initially not sufficiently electrocatalytically active for the reaction of OER in an alkaline environment, after being reduced, lead to the formation of finely dispersed nanoparticles of Ni-Fe alloys and  $\text{Ni}^0$ , improve the qualities intrinsically linked to the electronic transport or to the pseudo-capacitive ability of the catalysts which reflected into an increased activity in the OER reaction compared to the initial catalysts.

8) Catalysts composed of mixed metal oxides of Fe-Ce-Ni can be encapsulated inside carbon nanofibers through the decomposition process of methanol. These CNFs have very interesting morphological characteristics, and can be used in the oxygen evolution reaction and very low overpotential values at high anode currents, which would make them excellent catalysts for the hydrogen evolution reaction and the production of the same gas at level sustainable.

9) The correct choice of the reaction environment considerably influences the catalytic yield in the APR-EG reaction. The use of an alkaline environment ( $\text{pH} = 14$ ) instead of the standard ( $\text{pH} = 7$ ) about double increases the percentage of ethylene glycol converted and increases the hydrogen yield by about five times, for the 510SnNi-CZ\_red catalyst.

10) The addition of Sn, allows a targeted choice in the formation of NiSn alloys. The  $\text{Ni}_3\text{Sn}$  alloys (formed in the 2.510SnNi-CZ\_red and 510SnNi-CZ\_red catalysts) are extremely more active and more selective in APR of ethylene glycol than the  $\text{Ni}_3\text{Sn}_2$  alloys formed in the 1010SnNi-CZ\_red catalyst. The relative abundance of  $\text{Sn}^{4+}$  ions still dispersed in the  $\text{Ce}(\text{Zr})\text{O}_2$  support after the reduction process heavily influences the overall hydrogen yield of the reaction. The currently most effective combination for the APR-EG process was therefore found in the 510SnNi-CZ\_red catalyst.

11) From the analysis of the gaseous and liquid mixture produced by the reaction it is possible to see how the fragmentation paths of ethylene glycol on the surface of the

monometallic catalysts in Sn and Ni, are very different and in the case of the former lead to the formation of short-chain hydrocarbons (saturated and unsaturated). It can be said that the bimetallic catalytic combination is an average between the two mechanisms and that summarily benefits synergistically from the best of the two.

12) It was possible to observe the synergistic action between ceria-zirconia support and the active metal phase, carried out by the capture by the support, of the carbonaceous component produced and the probable unbalancing of the reaction equilibria related to the formation of products in the APR-EG reaction.

### **MAIN CONTRIBUTIONS:**

1) For the first time, the hydrothermally obtained Fe-Ce mixed oxides were considered as a continuous set of ceria- and hematite- like entities, which proportion could be varied by the Fe/Ce ratio and the preparation conditions used.

2) For the first time the superimposition of the effects of Ni-Fe-Ce composition and the influence of the reaction medium was considered in development of highly active in methanol decomposition catalysts. A complex mechanism of regulation of the amount of defects in the ceria-iron oxide interface, stabilization of small Ni particles by “encapsulation” in carbon filaments and changes in the reaction mechanism due to the formation of metal carbides and alloys is assumed.

3) For the first time, the methanol decomposition process was used not only as a mere hydrogen production process, but also as a synthetic process to promote the encapsulation of Fe-Ce-Ni catalysts and increase their electrocatalytic activity. Effectively proving, the potential within a circular economy for hydrogen production, in which "spent" catalysts from reforming processes can be used directly for electrocatalytic purposes.

4) For the first time, for the aqueous-phase reforming reaction of ethylene glycol, it was reported in the same paper, the combination of the changes in catalytic activity and selectivity brought about by both the correct choice of active Ni-Sn metal alloys, based on the different relative concentration of tin, and the correct choice of reaction environment. The combination of these two factors heavily influences the hydrogen yield and selectivity toward the methanation reaction.

### **SCIENTIFIC PUBLICATIONS:**

1. “*Mesoporous Ce–Fe–Ni nanocomposites encapsulated in carbon-nanofibers: Synthesis, characterization and catalytic behavior in oxygen evolution reaction*”.

Consolato Rosmini, Tanya Tsoncheva, Daniela Kovatcheva, Nikolay Velinov, Hristo Kolev, Daniela Karashanova, Momtchil Dimitrov, Boyko Tsyntsarski, David Sebastián, María Jesús Lázaro. **Carbon**, **196 (2022) 186-202. DOI/10.1016/j.carbon.2022.04.036.**

2. “*Nickel-Decorated Mesoporous Iron–Cerium Mixed Oxides: Microstructure and Catalytic activity in Methanol Decomposition*”.

Tanya Tsoncheva, Consolato Rosmini, Mihail Mihaylov, Jiří Henych, Kristina Chakarova, Nikolay Velinov, Daniela Kovacheva, Zuzana Němečková, Martin Kormunda, Radostina Ivanova, Ivanka Spassova, and Konstantin Hadjiivanov. **ACS Applied Materials and Interfaces**, **14 (2021) 873–890. DOI/10.1021/acsami.1c19584.**

3. “*Formation of Catalytic Active Sites in Hydrothermally Obtained Binary Ceria–Iron Oxides: Composition and Preparation Effects*”.

Tanya Tsoncheva, Consolato Rosmini, Momtchil Dimitrov, Gloria Issa, Jiri Henych, Zuzana Němečková, Daniela Kovacheva, Nikolay Velinov, Genoveva Atanasova, and Ivanka Spassova. **ACS Applied Materials & Interfaces**, **13 (2021) 1838-1852. DOI/10.1021/acsami.0c16326.**

### **CITATIONS LIST:**

On the work " *Formation of Catalytic Active Sites in Hydrothermally Obtained Binary Ceria–Iron Oxides: Composition and Preparation Effects* " **4 citations** were reported:

1) "Pt-doped  $\alpha$ -Fe<sub>2</sub>O<sub>3</sub> mesoporous microspheres with low-temperature ultra-sensitive properties for gas sensors in diabetes detection". Zhaohui Lei, Pengfei Cheng, Yinglin Wang, Luping Xu, Li Lv, Xu Li, Shanfu Sun, Xidong Hao, Yaoqiong Zhang, Yue Zhang, Zhi Weng, **Applied Surface Science**, 607 (2023), 154558. <https://doi.org/10.1016/j.apsusc.2022.154558>.

(Currently online, publication date relative to the print edition of the journal).

2) "Multifunctional CeO<sub>2</sub> incorporated Fe<sub>2</sub>O<sub>3</sub> anchored on a rich porous structured carbon backbone for supercapacitors and adsorption of acid orange II". Hang Zhang, Lijuan Xia, Jianping Tang, Yuan Li, Lei Wang, Chuying Ouyang, Shengliang Zhong. **Materials Advances**, 3 (2022) 6818-6825. <https://doi.org/10.1039/D2MA00377E>.

3) "Research Progress of a Composite Metal Oxide Catalyst for VOC Degradation". Kai Zhang, Honglei Ding, Weiguo Pan, Xiaotian Mu, Kaina Qiu, Junchi Ma, Yuetong Zhao, Jie Song, and Ziyi Zhang. **ACS-Environmental Science & Technology**, 56 (2022), 9220-9236. DOI: 10.1021/acs.est.2c02772.

4) "Solvothermal Synthesis Routes to Substituted Cerium Dioxide Materials". James W. Annis, Janet M. Fisher, David Thompsett, Richard I. Walton. **Inorganics**, 9 (6) (2021),40. <https://doi.org/10.3390/inorganics9060040>.

## **LIST PARTICIPATION IN SCIENTIFIC CONFERENCES**

1) “*Carbon-Nanofibers Encapsulated Fe-Ce-Ni mesoporous nanoparticles: Synthesis, morphological studies and catalytic behavior for the oxygen evolution reaction in an alkaline medium*”. Consolato Rosmini, Tanya Tsoncheva, Daniela Kovatcheva, Nikolay Velinov, Daniela Karashanova, David Sebastián, María Jesús Lázaro.

**Third Workshop on Size-Dependent Effects in Materials for Environmental Protection and Energy Application (SizeMat3). September 12 – 15 (2021), Pomorie, Bulgaria.**

2) “*Nickel decorated mesoporous iron-cerium mixed oxides as catalysts for sustainable environmental protection*”. Consolato Rosmini, Tanya Tsoncheva, Mihail Mihaylov, Jiří Henych, Kristina Chakarova, Nikolay Velinov, Daniela Kovacheva, Zuzana Němečková, Martin Kormunda, Radostina Ivanova, Ivanka Spassova, Konstantin Hadjiivanov.

**Eighth National Crystallographic Symposium with International Participation. September 1–4, 2021, Varna, Bulgaria.**

3) “*Carbon foam supported Co-Zn ferrite nanoparticles as catalysts for methanol decomposition: Effect of Co/Zn ratio*”. Consolato Rosmini, Tanya Tsoncheva, Radostina Ivanova, Daniela Kovacheva, Ivanka Spassova, Nikolay Velinov.

**Second International Conference on Reaction Kinetics, Mechanisms and Catalysis. May 20-22, Budapest, Hungary.**

4) “*Effects of different synthesis methodologies of Fe-Ce oxide catalysts for methanol decomposition*”. Consolato Rosmini, Tanya Tsoncheva, Momtchil Dimitrov, Daniela Kovatcheva, Nikolay Velinov.

**XIII Spring Seminar – Webinar of young scientists and doctoral students from the BAS. June 22-24, 2020, Sofia, Bulgaria.**

5) “*Effect of the composition of binary Fe-Ce oxide catalysts for methanol decomposition*”.

Consolato Rosmini, Momtchil Dimitrov, Daniela Kovatcheva, Nikolay Velinov, Tanya Tsoncheva.

**Second International School on NanoAlloys (ISNA-2) within the BIKE MSCA ITN project. January 20 – 25, 2020 Pisa, Italy.**

6) “*Ni-Fe and Ni-Sn mesoporous catalysts for environmental protection*”. Consolato Rosmini (30 minutes’ plenary presentation). **Workshop on Catalysis and design of advanced reactors” and “2<sup>nd</sup> Annual Network Symposium (BIKE-project). December 13-16, 2021 Barcelona, Spain.**

7) “Advanced iron and nickel based materials for the safe production and storage of hydrogen”. Consolato Rosmini (30 minutes’ plenary presentation). **“3<sup>rd</sup> Annual Network Symposium (BIKE-project). September 05-09, 2022 Milano, Italy.**

**PERIODS OF SCIENTIFIC SPECIALIZATION IN FOREIGN INSTITUTIONS  
WITHIN THE 'THESIS PROGRAM:**

July – September 2022: Secondment-training, within the BIKE-MSCA project, at " Institut für Technische Chemie und Polymerchemie” of the Karlsruhe Institute of Tecnology (KIT) and ANKA synchrotron light source , With the specific purpose of: Operando and ex-situ XAS characterization, of catalysts for aqueous phase reforming of polyols. **Karlsruhe (Germany).**

January - March 2021: Secondment-training, within the BIKE-MSCA project, at "Department of Chemical Engineering” of the Norwegian Institute of Tecnology (NTNU), With the specific purpose of: Testing of catalysts for the aqueous phase reforming reaction, in batch reactor and proceeded with a further modification and testing of the above catalysts to increase their catalytic properties. **Trondheim (Norway).**

March – June 2020: Secondment-training, within the BIKE-MSCA project, at "Instituto de Carboquímica (CSIC) of Zaragoza’”. With the specific purpose of: Synthesis and testing of novel mixed Oxides and carbomaterials as catalysts for the reaction of water electrolysis and hydrogen production. **Zaragoza (Spain).**